

IAC-22,C1,2,5,x68843

Optimal Actuator-based Attitude Maneuvering of Constrained Spacecraft via Motion Planning Algorithms

Riccardo Calao^{a,*} and Hanspeter Schaub^b

^a *Ph.D. student, Ann and H.J. Smead Department of Aerospace Engineering Sciences, University of Colorado, Boulder, 3775 Discovery Drive, Boulder, CO, 80303, riccardo.calaon@colorado.edu*

^a *Professor and Department Chair, Schaden Leadership Chair, Ann and H.J. Smead Department of Aerospace Engineering Sciences, University of Colorado, Boulder, 431 UCB, Colorado Center for Astrodynamics Research, Boulder, CO, 80309. AAS Fellow, AIAA Fellow, hanspeter.schaub@colorado.edu*

* Corresponding Author

Abstract

Maneuvering a spacecraft that is subject to hard rotational constraints is a nontrivial challenge. This paper exploits the properties of the Modified Rodrigues Parameters (MRPs) to yield a nonsingular sampling of the attitude space of a spacecraft, from which a undirected graph of constraint-compliant attitude waypoints is obtained. A path planning algorithm is used to compute a valid waypoint-based path in the graph, and NURBS functions are used to obtain a smooth, twice-differentiable reference trajectory from such constraint-compliant waypoint sequence. This paper considers the fully-coupled dynamic equations of a spacecraft actuated using ~~different~~ sets of reaction wheels, whose equations of motion can be integrated accurately thanks to the time-continuous nature of NURBS functions. This leads to the definition of new cost functions for the pathfinding algorithm that are based on the actuator dynamics, their control torque capabilities and power consumption.

1. Introduction

When a spacecraft is subject to hard rotational constraints, reorienting the spacecraft while ensuring that the constraints are being respected poses significant challenges. Such constraints often take the shape of conical keep-out zones and keep-in zones. This is, for example, the case of a sensitive instrument with an axisymmetric field of view, that should never overlap with the inertial direction of a bright celestial object such as the Sun. This case is represented by an inertial keep-out zone. Vice versa, when a body-fixed direction in the spacecraft must remain within a certain angular distance from a certain celestial object, there is a conical keep-in zone. This can be the case for solar arrays or sun sensors, that must always point at the Sun.

Solutions to the constrained attitude maneuvering problem can be broadly categorized into two groups: potential-function-based solutions and path-planning-based solutions. Potential-function-based solutions typically feature an artificial potential function that is composed of an attractive potential, which steers the spacecraft towards the desired attitude, and of a repulsive potential, which steers the spacecraft away from constraint boundaries.¹⁻⁴ These approaches are usually both easy to implement and computationally fast, and they output a smooth, time-dependent reference trajectory. On the other hand, such approaches fail in the presence of multiple overlap-

ping constraints, oddly-shaped constraints, and particular symmetries. Path-planning-based approaches do not usually suffer from any of these shortcomings provided that the workspace is mapped adequately. On the other hand, most path-planning algorithms rely on some form of workspace discretization, which leads to a waypoint-based solution: therefore, the reference is often provided in terms of a series of constraint-compliant attitude waypoints, rather than a smooth, time-dependent reference trajectory.⁵⁻⁸ More recent work by Tan et al.⁹ and Calao et al.^{10,11} are based on the attitude discretization that is typical of path-planning-based approaches with some forms of waypoint interpolation or approximation to obtain a time-dependent reference trajectory, which can accurately be tracked by the spacecraft.¹² Moreover, in these latest approaches, information regarding the mass properties and dynamic state of the spacecraft can be incorporated into the pathfinding algorithm to yield an effort-optimal solution.

This paper adopts the same attitude discretization in the Modified Rodrigues Parameters (MRPs) space presented in References 10, 11, but enhances the cost function formulation adopted by the effort-based A* solution, to provide a more insightful estimate on the cost required to perform the attitude maneuver. In particular, the time-dependent nature of the fitting NURBS curves is exploited to yield very accurate integration of the actuators' equa-

tions of motion, from which it is possible to compute the instantaneous power consumption required to track the reference trajectory.

This paper is structured as follows: Section 2. summarizes the properties of MRPs, the constrained attitude workspace sampling, and the properties of NURBS curves as they have been used in previous contributions. Section 3. introduces the actuator dynamics equations, and outlines how to leverage the continuous-time properties of NURBS curves to yield a precise integration of such equations. Section 4., based on the enhanced model of the spacecraft and actuators, presents new cost functions that are used for the A* effort-based graph search. Section 5. presents numerical results and simulations where these cost functions are tested and compared, while conclusions are drawn in Section 6..

2. MRP attitude discretization and NURBS fit

2.1 Modified Rodrigues Parameters

The Modified Rodrigues Parameters (MRPs) are a set of coordinates used to represent the attitude of a rigid body that can rotate in the $SO(3)$ space. One MRP set is defined, from the Principal Rotation Vector (PRV) and Principal Rotation Angle (PRA) with respect to a reference orientation (\hat{e}, Φ) , as:

$$\sigma = \frac{1}{1 + \cos(\Phi/2)} \begin{Bmatrix} e_1 \sin(\Phi/2) \\ e_2 \sin(\Phi/2) \\ e_3 \sin(\Phi/2) \end{Bmatrix} = \hat{e} \tan\left(\frac{\Phi}{4}\right). \quad (1)$$

Equation (1) shows that the MRP formulation, being a minimal 3D set, has a singularity at $\Phi = \pm 2\pi$, which describes rotations of ± 360 degrees from the reference attitude. Such singularity can be avoided considering the shadow set (\hat{e}, Φ') , with $\Phi' = 2\pi - \Phi$, describing the same attitude with respect to the reference, but performing the 'long' rotation, and assuming, without loss of generality, that $0 \leq \Phi \leq \pi$ and $\pi \leq \Phi' \leq 2\pi$. This gives the shadow MRP set:

$$\sigma^S = \hat{e} \tan\left(\frac{\Phi'}{4}\right) = -\frac{\sigma}{\sigma^2} \quad (2)$$

where $\sigma^2 = \|\sigma\|^2$. Analyzing Equations (1) and (2) it is possible to observe that all the MRP sets contained within a unit sphere centered at the origin represent the space of all possible short rotations ($|\Phi| \leq \pi$) from the reference, whereas the points that lie outside the unit sphere represent the respective long rotations. Because all the existing attitudes, except rotations of $\Phi = 0, \pm 2\pi$, are mapped twice into MRP space, it is possible to restrict the operational domain to the points that lie within the unit sphere. This automatically removes the singularity from the operational domain of this paper. Rotations of $\Phi = 0, \pm 2\pi$ are only mapped to the origin of the MRP space, which is also included in the unit sphere. It should be noted that, on the

other hand, this operation introduces a discontinuity in the attitude description: when a rotation larger than 180 degrees occurs, the relative MRP set approaches the boundary of the unit sphere and, after intersecting it, it 'reappears' on the diametrically opposite side of the sphere.

The correlations between MRP derivatives $\dot{\sigma}$ and $\ddot{\sigma}$ and the spacecraft's angular rate and acceleration vectors ${}^B\omega_{B/\mathcal{N}}$ and ${}^B\dot{\omega}_{B/\mathcal{N}}$ with respect to the inertial frame \mathcal{N} , expressed in the spacecraft's body frame \mathcal{B} , are presented. Angular rates and accelerations are always intended as those of the body frame with respect to the inertial frame, and are expressed in body-frame coordinates, therefore, for ease of notation, such vectors are from now on referred to as ω and $\dot{\omega}$. The differential kinematic equations for the angular rates are:

$$\dot{\sigma} = \frac{1}{4}[B(\sigma)]\omega \quad (3)$$

$$\omega = 4[B(\sigma)]^{-1}\dot{\sigma} \quad (4)$$

where the $[B(\sigma)]$ and $[B(\sigma)]^{-1}$ matrices are:

$$[B(\sigma)] = (1 - \sigma^2)[\mathbf{I}_{3 \times 3}] + 2[\tilde{\sigma}] + 2\sigma\sigma^T \quad (5)$$

$$[B(\sigma)]^{-1} = \frac{1}{(1 + \sigma^2)^2}[B(\sigma)]^T \quad (6)$$

and $[\tilde{\sigma}]$ is the skew-symmetric matrix obtained from σ . The equations for the angular accelerations are obtained differentiating Equations (3) and (4):

$$\ddot{\sigma} = \frac{1}{4} \left([B(\sigma)]\dot{\omega} + [\dot{B}(\sigma, \dot{\sigma})]\omega \right) \quad (7)$$

$$\dot{\omega} = 4[B(\sigma)]^{-1} \left(\ddot{\sigma} - [\dot{B}(\sigma, \dot{\sigma})][B(\sigma)]^{-1}\dot{\sigma} \right). \quad (8)$$

where:

$$[\dot{B}(\sigma, \dot{\sigma})] = (-2\sigma^T\dot{\sigma})[\mathbf{I}_{3 \times 3}] + 2[\dot{\tilde{\sigma}}] + 2(\sigma\dot{\sigma}^T + \dot{\sigma}\sigma^T). \quad (9)$$

More details on MRPs and their properties are found in Reference 13.

2.2 Workspace discretization and constraint representation

The attitude space is restricted to a unit MRP sphere centered at the origin. Such sphere is sampled with a uniform, 3D cartesian grid consisting of equally-spaced nodes. Each node is connected to a maximum of 26 neighboring nodes. This does not strictly apply to boundary nodes, placed along the $\sigma = 1$ boundary of the sphere: such nodes, additionally, are connected to the neighboring nodes of their respective shadow set nodes to allow for the discontinuity around $\Phi = \pm\pi$. The combination of nodes and connecting edges constitutes an undirected graph that can be searched for a valid path between the

starting node (initial attitude) and goal node (final attitude). Such path, in its coarse form, is just a sequence of waypoints. Figure 1 shows the discretized sphere with two paths, one that features a discontinuity and one that does not. N , defined as the number of nodes per semi-axis, parameterizes the grid density. Figure 2 shows how a set of three keep-out zones map to the equivalent obstacles in MRP space: the nodes falling into such keep-out zones are removed from the graph and therefore automatically avoided by the pathfinding algorithm.

For a more thorough description of the MRP discretization, see Reference 10.

2.3 Waypoint fitting via NURBS curves

NURBS (Non-Uniform Rational B-Spline) curves are parametric, piecewise polynomial functions that are particularly suitable to approximating large sets of data without diverging. The piecewise nature of these curves makes it such that the polynomial order p is chosen by the user, instead of being determined by the number of data to fit.^{14,15} Moreover, a NURBS curve of degree p is C^{p-1} : in this paper, the order used is $p = 4$, which is enough to ensure the continuity and differentiability of the attitude, angular rates and angular accelerations of the spacecraft at all times. The general expression of a NURBS curve is:

$$\sigma(u) = \sum_{i=0}^n N_{i,p}(u)P_i \quad (10)$$

with $u \in [0, 1]$ being the dimensionless time parameter along the curve, P_i are the $n + 1$ control points, that must be computed, and $N_{i,p}(u)$ are the basis functions of order p whose linear combination constitutes the curve. The basis functions are computed using De Boor's recursive

algorithm:¹⁶

$$N_{i,0}(u) = \begin{cases} 1 & \text{if } u_i \leq u < u_{i+1} \\ 0 & \text{otherwise} \end{cases}$$

$$N_{i,p}(u) = \frac{u - u_i}{u_{i+p} - u_i} N_{i,p-1}(u) + \frac{u_{i+p+1} - u}{u_{i+p+1} - u_{i+1}} N_{i+1,p-1}(u). \quad (11)$$

To compute the basis functions, it is also necessary to define the $m + 1$ knots:

$$U = \{ \underbrace{0, \dots, 0}_{p+1}, u_{p+1}, \dots, u_{m-p-1}, \underbrace{1, \dots, 1}_{p+1} \} \quad (12)$$

and the dimensionless times \bar{u}_k for $k = 0, \dots, q$ with $q + 1$ being the number of waypoints, at which each waypoint is encountered along the curve.

Four control points, P_0, P_1, P_{n-1} and P_n are always determined based on the knowledge of the initial and final attitude, σ_0 and σ_q , and from the initial and final angular velocities ω_0 and ω_q , from which MRP rates σ'_0 and σ'_q are obtained using Equation (3). With these pieces of information the following 4×4 system is set up:

$$\begin{cases} N_{0,p}(0)P_0 & = \sigma_0 \\ N'_{0,p}(0)P_0 + N'_{1,p}(0)P_1 & = \sigma'_0 \\ N'_{n-1,p}(1)P_{n-1} + N'_{n,p}(1)P_n & = \sigma'_q \\ N_{n,p}(0)P_n & = \sigma_q \end{cases} \quad (13)$$

where the $N_{i,p}(u)'$ terms are the derivatives of the basis functions. The remaining $n - 3$ control points can be obtained through a linear system of the form:

$$NP = \rho \quad (14)$$

where P is a $n - 3$ vector, σ is a $q - 1$ vector, and N is a $q - 1 \times n - 3$ matrix whose entries are the basis functions $N_{i,p}(u)$. When the number of control points is chosen such that $n = q + 2$, the system in Equation (14) is determined and the solution results in perfect interpolation. Alternatively, the system can be solved via pseudo-inverse, in which case a least-squares fit of the waypoints is obtained. It should be noted that Equations (13) and (14) actually represent 3 equations each, given that the control points exist in three-dimensional space.

More information on how to fit NURBS curves to MRP waypoint sequences can be found in References 10, 11.

3. Actuator dynamics

In 10, 11 the control effort is defined based on the Euler's equations of motion:

$$L = [I]\dot{\omega} + \omega \times ([I]\omega) \quad (15)$$

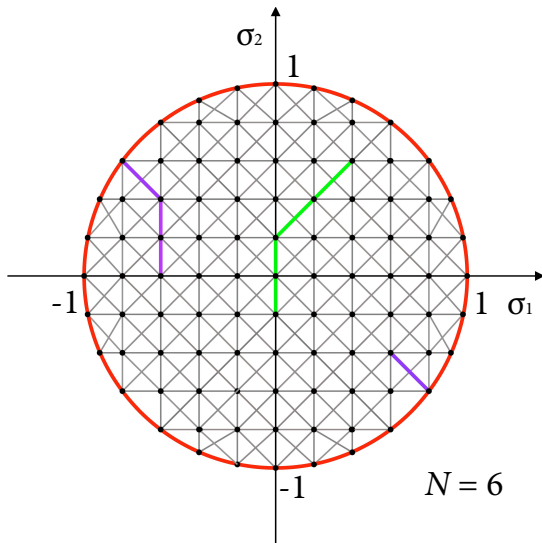


Fig. 1: 2D MRP grid with two shortest-distance paths: i) green: no MRP discontinuity; ii) purple: MRP discontinuity¹⁰

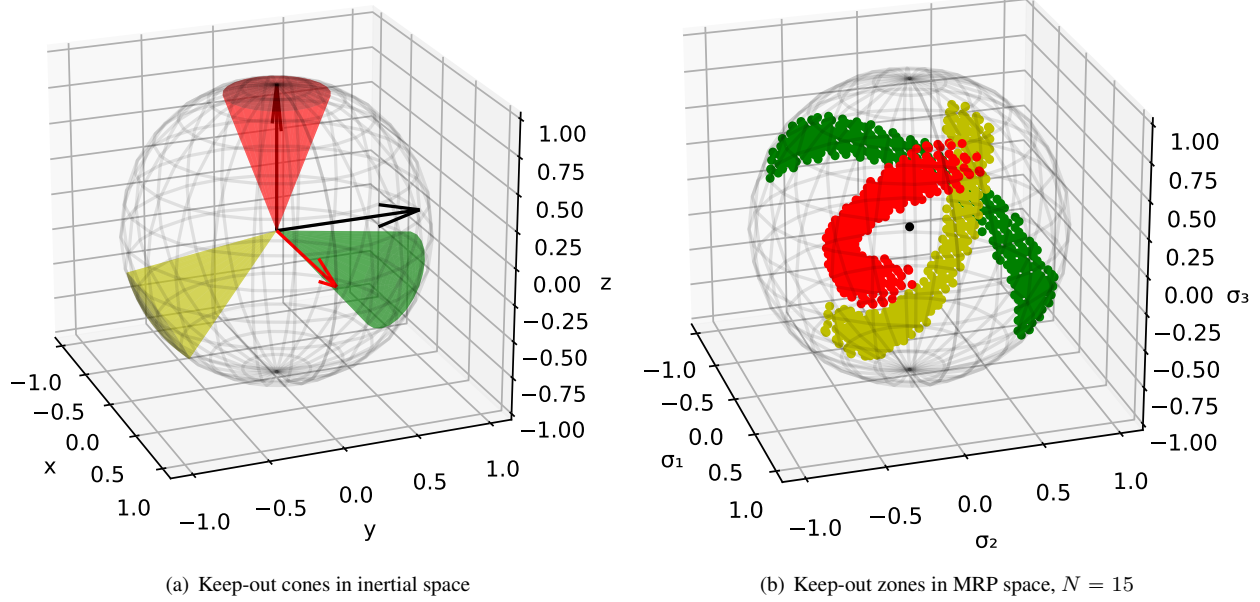


Fig. 2: Three general keep-out constraints, $\beta = 20$ degrees¹⁰

with $[\mathbf{I}]$ being the inertia tensor of the spacecraft expressed in the body frame. The formulation in Equation (15), however, only accounts for the control effort required to track the reference trajectory based on the spacecraft's inertia properties, but it does not consider the actuators that deliver the torque, nor their dynamics and inertias. For a spacecraft with M reaction wheels and no external disturbances, the equations of motion are given by:¹³

$$[\mathbf{I}_{RW}]\dot{\boldsymbol{\omega}} = -\boldsymbol{\omega} \times ([\mathbf{I}_{RW}]\boldsymbol{\omega} + [\mathbf{G}_s]\mathbf{h}_s) - [\mathbf{G}_s]\mathbf{u}_s \quad (16)$$

where $[\mathbf{G}_s] = [\hat{\mathbf{g}}_{s_1}, \dots, \hat{\mathbf{g}}_{s_M}]$ is a $3 \times M$ matrix containing the body-frame directions of the RW spin axes in its columns. The term $[\mathbf{I}_{RW}]$ is used to account for the inertias of the wheels as they rotate with the spacecraft, and it is computed as:

$$[\mathbf{I}_{RW}] = [\mathbf{I}] + \sum_{i=1}^M I_{w_t} (\hat{\mathbf{g}}_{t_i} \hat{\mathbf{g}}_{t_i}^T + \hat{\mathbf{g}}_{g_i} \hat{\mathbf{g}}_{g_i}^T) \quad (17)$$

where I_{w_t} is the inertia of the axisymmetric wheel about a transverse axis, and $\hat{\mathbf{g}}_{t_i}$ and $\hat{\mathbf{g}}_{g_i}$ are the other two axes of the reaction wheel frame. Moreover:

$$\mathbf{h}_s = \left\{ \begin{array}{c} I_{w_s}(\omega_{s_1} + \Omega_1) \\ \vdots \\ I_{w_s}(\omega_{s_M} + \Omega_M) \end{array} \right\} \quad \text{with} \quad \omega_{s_i} = \hat{\mathbf{g}}_{s_i}^T \boldsymbol{\omega} \quad (18)$$

is the M -dimensional vector containing the angular momenta of each wheel. In these expressions, Ω_i are the relative angular velocities of the wheels with respect to

the spacecraft. The assumption is made that all wheels have the same inertia I_{w_s} about the spin axis. \mathbf{u}_s is a M -dimensional vector containing the actuating motor torques to each reaction wheel. The motor torques as functions of time required to track the trajectory can be computed as:

$$\mathbf{u}_s = -[\mathbf{G}_s]^T ([\mathbf{G}_s][\mathbf{G}_s]^T)^{-1} ([\mathbf{I}_{RW}]\dot{\boldsymbol{\omega}} + \boldsymbol{\omega} \times ([\mathbf{I}_{RW}]\boldsymbol{\omega} + [\mathbf{G}_s]\mathbf{h}_s)) \quad (19)$$

where the minimum-norm solution is computed, using the pseudo-inverse of $[\mathbf{G}_s]$, in the presence of a redundant ($M > 3$) reaction wheel set. With exactly three reaction wheels, the matrix $[\mathbf{G}_s]$ is invertible, assuming that the spin axes of the wheels are linearly independent. For redundant sets of reaction wheels, other solutions can be adopted other than the minimum norm, given that the problem of mapping a three-dimensional torque onto a four or more spin axes is underdetermined. Another approach, for example, allows to compute the motor torques that minimize the instantaneous wheel power consumption.¹⁷ The motor torques obey the following dynamic equation:

$$\mathbf{u}_s = I_{w_s} \left(\dot{\boldsymbol{\Omega}}_i + [\mathbf{G}_s]^T \dot{\boldsymbol{\omega}} \right) \quad (20)$$

which applies to each one of the reaction wheels. Equation (19) allows to compute the wheel torques required to track the reference trajectory; subsequently, inverting Equation (20) gives the derivative of the wheel speeds $\dot{\boldsymbol{\Omega}}$. Knowing the wheel speeds at the initial time $\boldsymbol{\Omega}(t_0)$, it is possible to apply the knowledge of the wheel accelerations to integrate the wheel speeds over time. A simple

forward Euler integration method gives:

$$\Omega(t_{n+1}) = \Omega(t_n) + (t_{n+1} - t_n)\dot{\Omega}(t_n) \quad (21)$$

however, such simple approach can often yield numerically imprecise results. Specifically, when tracking a rest-to-rest maneuver with wheels initially at rest, it is observed that the Euler integration results in nonzero final wheel speeds, due to numerical errors. The final wheel speeds being nonzero means that the total angular momentum of the spacecraft system is not conserved, in the absence of an external torque. A more robust integration technique is obtained by means of a 4th-order Runge-Kutta (rk4) algorithm. For this method, let's define the function $\dot{\Omega} = f(t, \Omega)$ as a combination of Equations (19) and (20):

$$f(t, \Omega) = -\frac{[\mathbf{G}_s]^T ([\mathbf{G}_s][\mathbf{G}_s]^T)^{-1}}{I_{w_s}} ([\mathbf{I}_{RW}]\dot{\omega} + \omega \times ([\mathbf{I}_{RW}]\omega + [\mathbf{G}_s]\mathbf{h}_s)) - [\mathbf{G}_s]^T \dot{\omega} \quad (22)$$

where the contribution of the wheel speeds Ω is included in the \mathbf{h}_s term, as per Equation (18). Knowing the wheel speeds at the instant $\Omega(t_n) = \Omega_n$, the integration proceeds calculating the four coefficients:

$$\begin{aligned} \mathbf{k}_1 &= f(t_n, \Omega_n) \\ \mathbf{k}_2 &= f\left(t_n + \frac{t_{n+1} - t_n}{2}, \Omega_n + \mathbf{k}_1 \frac{t_{n+1} - t_n}{2}\right) \\ \mathbf{k}_3 &= f\left(t_n + \frac{t_{n+1} - t_n}{2}, \Omega_n + \mathbf{k}_2 \frac{t_{n+1} - t_n}{2}\right) \\ \mathbf{k}_4 &= f(t_{n+1}, \Omega_n + \mathbf{k}_3(t_{n+1} - t_n)) \end{aligned} \quad (23)$$

from which the integrated wheels speeds at instant t_{n+1} are obtained as:

$$\Omega(t_{n+1}) = \Omega(t_n) + (t_{n+1} - t_n) \frac{\mathbf{k}_1 + 2\mathbf{k}_2 + 2\mathbf{k}_3 + \mathbf{k}_4}{6}. \quad (24)$$

Once the equations of motion of the reaction wheels are integrated, it is possible to define the instantaneous power required by the motor torque to actuate the wheels:

$$W_i = u_{s_i} \Omega_i. \quad (25)$$

In general, $W_i(t)$ can be either positive or negative, where $W_i > 0$ indicates that the wheel is acting as a power load, thus absorbing power from the spacecraft, while $W_i < 0$ that the wheel is acting as a power source. This is only realistic for systems with regenerative wheels, where the power used to brake the wheel's speed can be harvested and transferred back to the spacecraft.¹⁸

Figure 3 shows an example of a constraint-compliant reference trajectory computed using the metric-based A* algorithm. This simpler, faster version of A* computes

a solution based on the distance between nodes in MRP space, which means that the trajectory is not effort-optimal. Such trajectory is a rest-to-rest maneuver with an almost-constant angular rate norm of $\|\omega\| = 0.03$ rad/s, performed with a sensitive Star Tracker with a field of view of 20 degrees along the $\hat{\mathbf{b}}_x$ body axis, and two inertially-fixed bright celestial objects. Figure 4 shows the dynamics of the reaction wheels used to actuate the spacecraft. In particular, subfigure (a) is obtained using three RWs aligned with the principal inertia axes of the spacecraft, whereas subfigure (b) is obtained assuming a redundant set of four reaction wheels, along the positive and negative $\hat{\mathbf{b}}_x$ and $\hat{\mathbf{b}}_y$ semiaxes, and with a tilt angle of 30 degrees towards the positive $\hat{\mathbf{b}}_z$ semiaxis. In both cases, all RWs are actuated from an initial rest condition. As a proof of concept, it is possible to observe that all reaction wheel speeds converge to $\Omega = 0$ at the end of the maneuver: this is because the total angular momentum of the spacecraft and wheels system is zero. Since the final angular rate of the hub is zero, the wheel speeds also go to zero to ensure that the angular momentum is conserved. This is strictly true for the case with three reaction wheels. In the case with four reaction wheels, it could be possible to obtain nonzero final angular rates, for which the total cumulative angular momentum of the system is still zero: this could happen using a different torque mapping than the one presented in Equation (19), due to the existence of a one-dimensional null-space for the reaction wheel set.¹⁷

The final wheel speeds are still affected by integration errors; however, such integration errors are as small as 10^{-4} rad/s.

4. Effort-based graph search

The effort-based A* algorithm is outlined in Reference 10 and it uses intermediate trajectories to estimate the control effort required to track such trajectories. The control effort is used as the cost function to drive the search of the A* algorithm. The search is performed starting from the initial node σ_0 and exploring the neighboring nodes that are the most likely to yield the cost-optimal path. When the n -th node σ_n is being explored, an intermediate NURBS trajectory is computed using the set of waypoints $\{\sigma_0, \dots, \sigma_n, \sigma_t\}$, with σ_t being the target attitude. The cost function is defined as the sum of the cost-to-current-node $g(n)$ and a heuristic cost-to-goal $h(n)$. In Reference 10, 11 this cost function is defined as the integral over the trajectory time of the control torque defined in Equation (15):

$$C_0 = p(n) = g(n) + h(n) = \int_0^T \|\mathbf{L}\| dt \quad (26)$$

where $p(n)$ denotes the total priority of the node. As previously mentioned, the expression in Equation (15) is inaccurate, as it only factors in the spacecraft's inertias and

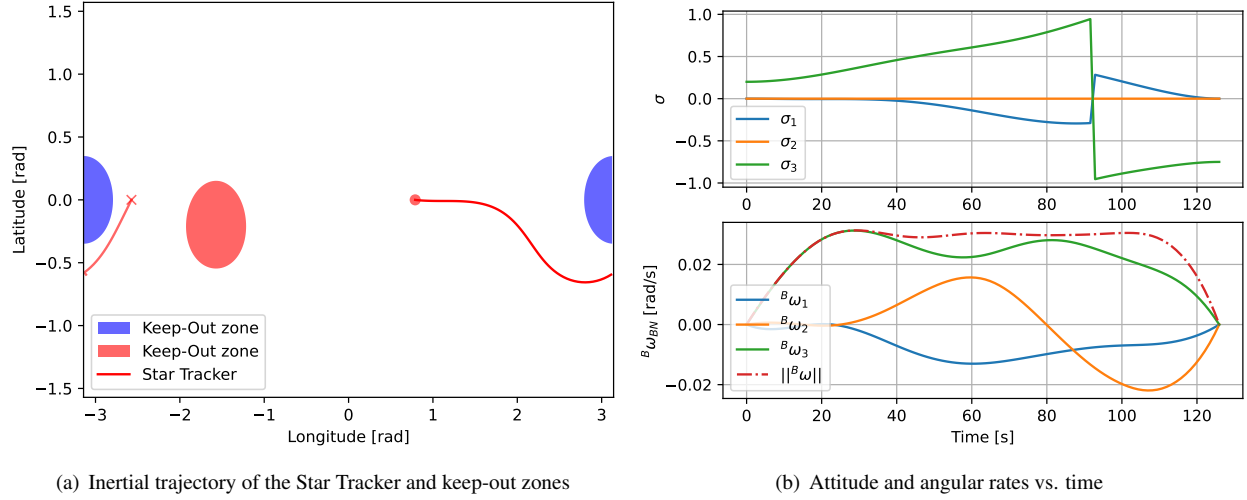


Fig. 3: Example trajectory computed with metric-based A^* , $N = 7$.

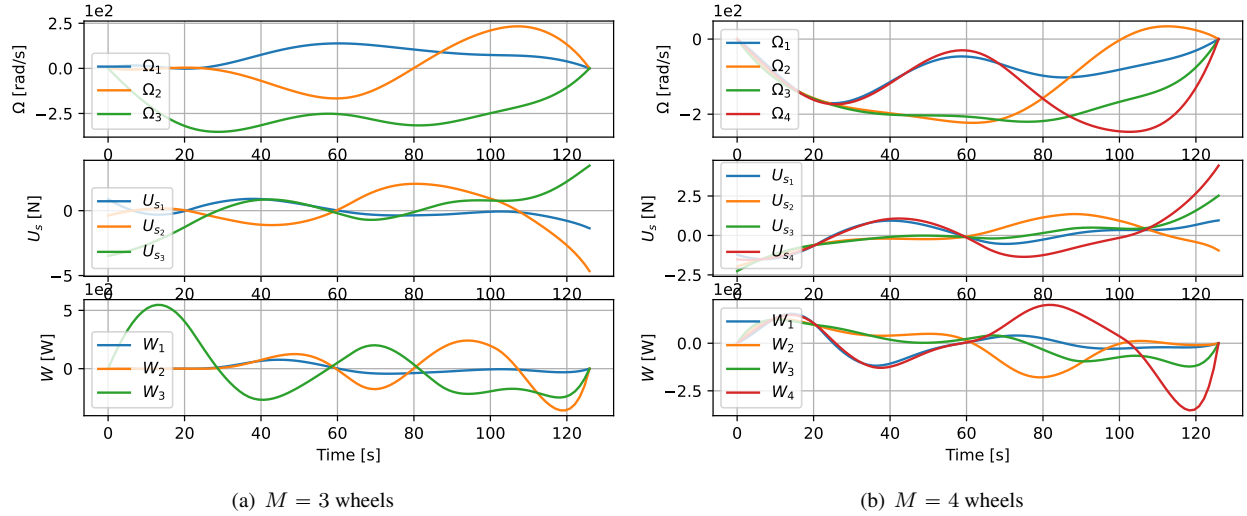


Fig. 4: Wheel speeds, wheel control torques and power required to track the trajectory in Figure 3

the tracked angular rates and accelerations of the hub, but not the actuators' inertias and angular momentum contributions. In this section, new cost functions are defined in order to factor the actuator dynamics into the effort-based graph search. The control-based cost functions can be enhanced using the result in Equation (16):

$$\begin{aligned}
 C_1 &= \int_0^T \|\mathbf{L}_r\| dt = \int_0^T \|\mathbf{G}_s \mathbf{u}_s\| dt \\
 &= \int_0^T \|\mathbf{I}_{RW} \dot{\boldsymbol{\omega}} + \boldsymbol{\omega} \times (\mathbf{I}_{RW} \boldsymbol{\omega} + \mathbf{G}_s \mathbf{h}_s)\| dt
 \end{aligned} \tag{27}$$

where the reaction wheels, their inertias, and the momentum build up on them are accounted for in the control torque \mathbf{L}_r .

The cost function can be modeled after the amount of energy required to actuate the spacecraft, obtained as the integral of the motor power in Equation (25). In this case, it is important to define what the motor power describes in terms of "cost" to the spacecraft's power system. With non-regenerative wheels, power is consumed by the motor torque to accelerate the wheels ($W_i > 0$); when the wheels brake ($W_i < 0$), the energy dissipated in the braking is lost. In this case, therefore, it makes sense to estimate the cost by integrating only over the time intervals in which the wheel powers are positive. For a set of M wheels, this can be done as:¹⁹

$$E = \sum_{i=1}^M \left[\int_0^T \frac{1}{2} (W_i + |W_i|) dt \right]. \tag{28}$$

In a case with regenerative wheels, the energy released by the wheels during the braking phase can be harvested and given back to the spacecraft. This means that the cost function should account for positive contributions due to the energy used to accelerate the wheels, minus the energy that is given back when decelerating the wheels. Assuming to have a regeneration efficiency factor $0 \leq \eta \leq 1$, the energy-based cost function for a general regenerative wheel is computed as:

$$C_2 = \sum_{i=1}^M \left[\int_0^T \left(\frac{1+\eta}{2} W_i + \frac{1-\eta}{2} |W_i| \right) dt \right], \quad (29)$$

where for $\eta = 0$ the case with zero regenerative capability is obtained. Thanks to some energy principle considerations, it is possible to observe that the energy-based cost function C_2 with perfect power regeneration is not suitable for all implementations. Specifically, with perfect power regeneration, it is:

$$\begin{aligned} C_2 &= \int_0^T I_{w_s} (\mathbf{u}_s \cdot \boldsymbol{\Omega}) dt \\ &= \int_0^T I_{w_s} \left(\dot{\boldsymbol{\Omega}} + [\mathbf{G}_s]^T \dot{\boldsymbol{\omega}} \right) \cdot \boldsymbol{\Omega} dt \\ &= I_{w_s} \int_0^T \boldsymbol{\Omega} \cdot d\boldsymbol{\Omega} + I_{w_s} \int_0^T \boldsymbol{\Omega} \cdot [\mathbf{G}_s]^T d\boldsymbol{\omega} \\ &= \frac{1}{2} I_{w_s} \boldsymbol{\Omega}(T) \cdot \boldsymbol{\Omega}(T) - \frac{1}{2} I_{w_s} \boldsymbol{\Omega}(0) \cdot \boldsymbol{\Omega}(0) \\ &\quad + \boldsymbol{\Omega}(T) \cdot [\mathbf{G}_s]^T \boldsymbol{\omega}(T) - \boldsymbol{\Omega}(0) \cdot [\mathbf{G}_s]^T \boldsymbol{\omega}(0). \end{aligned} \quad (30)$$

For a rest-to-rest maneuver, the total kinetic energy of the reaction wheels is likely to remain the same, as shown in Figure 4. This means that, for a case with perfect power regeneration ($\eta = 1$), it is also $C_2 = 0$. This means that using the C_2 cost function would be inconclusive, since all the trajectories would have the same zero cost, and the algorithm would not be able to prioritize any path over the others.

5. Numerical results

This last section implements the algorithms highlighted so far, and aims to test the validity of the method as well as to provide a comparison between results obtained using the different cost functions. The spacecraft properties used in the simulations are the following:

$${}^B[\mathbf{I}] = \begin{bmatrix} 1700 & 0 & 0 \\ 0 & 1700 & 0 \\ 0 & 0 & 1800 \end{bmatrix} \text{ kg/m}^2 \quad (31)$$

$$I_{w_s} = I_{w_t} = 0.16 \text{ kg/m}^2. \quad (32)$$

Simulations are set up for the spacecraft performing a non-rest-to-rest maneuver. In the first two cases, (a) and (b), the spacecraft is equipped with three reaction wheels

aligned with the principal body axes; in the latter two, (c) and (d), the spacecraft is equipped with four reaction wheels with the same configuration as described in Figure 4. For all four cases, the effort-based A* graph search is run with the three cost functions defined above: C_0 , C_1 and C_2 . The results obtained with the cost function C_0 are provided with the only scope of outlining how the newer approach is superior: in fact, in all four cases, the C_0 optimal solution is always associated with a higher C_1 cost than the C_1 -optimal solution. Because the latter is actually more accurate, it should always be preferred. Table 1 summarizes, for all four scenarios, the results obtained using each cost function as the driver for the effort-based A* solution, where zero power regeneration is assumed ($\eta = 0$). For each optimal solution, all three cost functions are evaluated and reported in the table for comparison. The different trajectories of the sensitive boresight are shown in Figure 5. For case (a) only, the C_1 -optimal and the C_2 -optimal trajectories coincide. In cases (a), (b) and (c), the inertia of the spacecraft plays the major role in determining the initial direction of the trajectory: the component along the $\hat{\mathbf{b}}_z$ axis of the initial angular velocity makes such that all the effort-optimal trajectories follow, at least initially, that direction. Figure 5 (d), on the contrary, shows a new, interesting behavior: the C_0 -optimal trajectory around $t = 0$ moves in a direction that is opposite to that of the C_1 - and C_2 -optimal trajectories. This highlights how the dynamics of the actuator can contribute significantly to the momentum and energy of the system, to the point where the effort computed based only on the properties of the spacecraft and the reference trajectory (C_0 function) can be a deceiving metric. For case (c), it is possible to observe that the C_2 -optimal solution is, in fact, not optimal with respect to C_2 , as the C_2 value computed for the C_1 -optimal solution is actually better. It can occasionally happen that these algorithms compute a sub-optimal solution: this is due to the way that NURBS curves affect the the update of the node priority inside the A* algorithm. It can happen that an intermediate trajectory, which would ultimately lead to the cost-optimal path, is associated with an intermediate cost that is higher than other suboptimal trajectories, therefore forcing the algorithm to explore other areas of the graph. This phenomenon, however, happens around solutions that are relatively close in cost to one-another. In this case, for example, the difference between the two is less than 1.5%.

The same four scenarios can be run with the C_2 -optimal algorithm, using varying levels of energy regeneration ($0 < \eta \leq 1$). The results are that, while the output C_2 cost is smaller for increasing values of η , as expected, the optimal trajectories for each case coincided with the trajectories computed using the C_2 -optimal algorithm with no power generation ($\eta = 0$). The reason why this happens is

Table 1: Simulation result data

(a)	$\omega_0 = [0, 0, 0.03]$ rad/s	$\Omega_0 = [0, 0, 0]$ rad/s		
C_0 -optimal:	$C_0 = 168.26$ Nms	$C_1 = 210.51$ Nms	$C_2 = 20297.77$ J	
C_1 -optimal:	$C_0 = 233.43$ Nms	$C_1 = 195.68$ Nms	$C_2 = 18857.63$ J	
C_2 -optimal:	$C_0 = 233.43$ Nms	$C_1 = 195.68$ Nms	$C_2 = 18857.63$ J	
(b)	$\omega_0 = [0, 0, 0.03]$ rad/s	$\Omega_0 = [500, 0, 0]$ rad/s		
C_0 -optimal:	$C_0 = 168.26$ Nms	$C_1 = 387.88$ Nms	$C_2 = 75831.74$ J	
C_1 -optimal:	$C_0 = 239.39$ Nms	$C_1 = 260.73$ Nms	$C_2 = 51244.46$ J	
C_2 -optimal:	$C_0 = 256.60$ Nms	$C_1 = 333.95$ Nms	$C_2 = 49957.61$ J	
(c)	$\omega_0 = [0, 0, 0.03]$ rad/s	$\Omega_0 = [100, -200, 0, 400]$ rad/s		
C_0 -optimal:	$C_0 = 168.26$ Nms	$C_1 = 207.82$ Nms	$C_2 = 27733.80$ J	
C_1 -optimal:	$C_0 = 168.26$ Nms	$C_1 = 194.27$ Nms	$C_2 = 27116.57$ J	
C_2 -optimal:	$C_0 = 233.43$ Nms	$C_1 = 245.10$ Nms	$C_2 = 27458.55$ J	
(d)	$\omega_0 = [0.03, 0, 0]$ rad/s	$\Omega_0 = [500, -200, -300, 400]$ rad/s		
C_0 -optimal:	$C_0 = 179.31$ Nms	$C_1 = 692.16$ Nms	$C_2 = 188392.80$ J	
C_1 -optimal:	$C_0 = 274.19$ Nms	$C_1 = 497.47$ Nms	$C_2 = 132997.65$ J	
C_2 -optimal:	$C_0 = 275.68$ Nms	$C_1 = 503.94$ Nms	$C_2 = 121433.82$ J	

probably that the amount of energy that is regenerated is a function of the initial and final states only. Therefore, the change in the cost function makes such that the node priority values in the A* algorithm change in absolute terms, but the priority order between them remains the same. In conclusion, the output of the effort-based graph search algorithm is the same. A more thorough analysis is needed to understand, from an energy and momentum balance perspective, why this happens.

6. Conclusions

This paper proposes a path-planning-based approach to maneuver a spacecraft that is subject to rotational constraints, in the form of keep-out and keep-in constraints. The solution is obtained applying an efficient graph-search algorithm that uses different cost functions to prioritize the search in the direction that is most likely to yield a cost-optimal solution. Such cost functions are modeled after the combined dynamics of the spacecraft and the momentum exchange devices that produce the internal

torques required to perform the maneuver. Emphasis is given to the nature of the NURBS curves used to convert a sequence of constraint-compliant attitude waypoints into smooth, time-dependent trajectories: this makes it possible to obtain a very precise integration of the actuators' equations of motion, by means of a 4th-order Runge-Kutta integrator.

Numerical results show how the enhanced cost functions, which include actuator dynamics, always outperform the cost function used in previous contributions, where such dynamics was neglected. One out of four cases reported shows that one of the trajectory is suboptimal with respect to the cost function that it was optimized for: this exposes some flaws in the methodology that will be addressed in the future; however, it seems that suboptimal behavior only in solutions that are very close to optimal, which further shows the validity of the method.

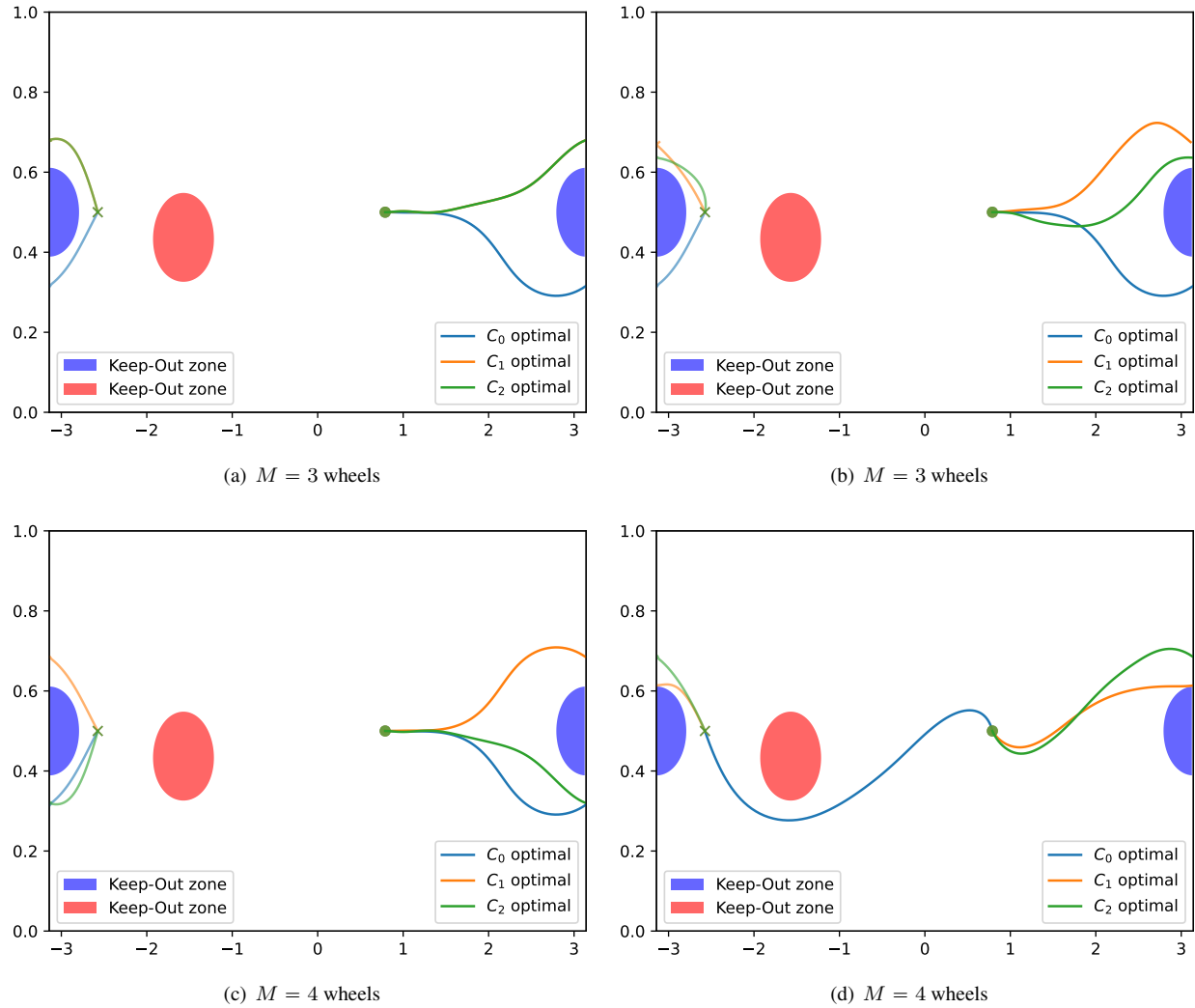


Fig. 5: Inertial trajectories of the sensitive boresight in different simulation scenarios

REFERENCES

- [1] Colin R McInnes. Large angle slew maneuvers with autonomous sun vector avoidance. *Journal of guidance, control, and dynamics*, 17(4):875–877, 1994.
- [2] Manuel Diaz Ramos and Hanspeter Schaub. Kinematic steering law for conically constrained torque-limited spacecraft attitude control. *Journal of Guidance, Control, and Dynamics*, 41(9):1990–2001, 2018.
- [3] Unsik Lee and Mehran Mesbahi. Spacecraft reorientation in presence of attitude constraints via logarithmic barrier potentials. In *Proceedings of the 2011 American Control Conference*, pages 450–455. IEEE, 2011.
- [4] Unsik Lee and Mehran Mesbahi. Feedback control for spacecraft reorientation under attitude constraints via convex potentials. *IEEE Transactions on Aerospace and Electronic Systems*, 50(4):2578–2592, 2014.
- [5] E Frazzoli, MA Dahleh, E Feron, and R Kornfeld. *A randomized attitude slew planning algorithm for autonomous spacecraft*, volume 4155. AIAA Reston, VA, 2001.
- [6] Henri C Kjellberg and E Glenn Lightsey. Discretized constrained attitude pathfinding and control for satellites. *Journal of Guidance, Control, and Dynamics*, 36(5):1301–1309, 2013.
- [7] Henri C Kjellberg and E Glenn Lightsey. Discretized quaternion constrained attitude pathfinding. *Journal of Guidance, Control, and Dynamics*, 39(3):713–718, 2015.
- [8] Sergei Tanygin. Fast autonomous three-axis constrained attitude pathfinding and visualization for boresight alignment. *Journal of Guidance, Control, and Dynamics*, 40(2):358–370, 2017.
- [9] Xiao Tan, Soulimane Berkane, and Dimos V Dimarogonas. Constrained attitude maneuvers on SO(3): Rotation space sampling, planning and low-level control. *Automatica*, 112:108659, 2020.

- [10] Riccardo Calaon and Hanspeter Schaub. Constrained attitude maneuvering via Modified-Rodrigues-Parameter-based motion planning algorithms. *Journal of Spacecraft and Rockets*, pages 1–15, 2022.
- [11] Riccardo Calaon and Hanspeter Schaub. Constrained attitude path planning via least squares MRP-based NURBS curves. In *AAS Astrodynamics Specialist Conference*, Charlotte, NC, Aug. 7–11 2022. Paper No. AAS 22-541.
- [12] Riccardo Calaon, Michael Trowbridge, and Hanspeter Schaub. A basilisk-based benchmark analysis of different constrained attitude dynamics planners. In *AIAA SciTech Forum*, San Diego, CA, Jan. 3–7 2022.
- [13] Hanspeter Schaub and John L Junkins. *Analytical Mechanics of Space Systems*. AIAA, 4 edition, 2018.
- [14] Les Piegl and Wayne Tiller. *The NURBS book*. Springer Science & Business Media, 1996.
- [15] Gerald E Farin and Gerald Farin. *Curves and surfaces for CAGD: a practical guide*. Morgan Kaufmann, 2002.
- [16] Carl De Boor. On calculating with b-splines. *Journal of Approximation theory*, 6(1):50–62, 1972.
- [17] Hanspeter Schaub and Vaios J Lappas. Redundant reaction wheel torque distribution yielding instantaneous L2 power-optimal spacecraft attitude control. *Journal of guidance, control, and dynamics*, 32(4):1269–1276, 2009.
- [18] Robin Blenden and Hanspeter Schaub. Regenerative power-optimal reaction wheel attitude control. *Journal of guidance, control, and dynamics*, 35(4):1208–1217, 2012.
- [19] Harleigh C Marsh, Mark Karpenko, and Qi Gong. Relationships between maneuver time and energy for reaction wheel attitude control. *Journal of Guidance, Control, and Dynamics*, 41(2):335–348, 2018.